X-ray absorption near-edge spectra and electronic structure of rhodium compounds

Yue Wu and D E Ellis

Department of Physics and Astronomy, Northwestern University, Evanston, IL 60208, USA

Abstract. Theoretical and experimental Rh L edge x-ray absorption near-edge spectra (XANES) in the compounds $RhCl_3$, Rh_2O_3 and $[Rh(CO)_2Cl]_2$ are presented. L_1 and $L_{2,3}$ pre-edge features (bound to bound state transitions) and near-edge features (continuum final states) are analysed and used to interpret experimental L_3 spectra. The self consistent-field local density theory was used to calculate charge densities and potentials, as well as densities of states in an embedded cluster approach. Multiple-scattering theory was used to determine the final states, and the absorption cross-section was calculated in the dipole approximation. Quantitative modelling of the absorption spectra permits detailed assignment of individual absorption features due to effective atomic configurations and local geometrical effects. The off-site Rh 4f resonance is a notable feature of the XANES which may be useful in characterizing Rh–Rh interaction.

1. Introduction

X-ray near-edge absorption spectroscopy (XANES) provides a local probe of atomic configuration and neighbouring site potentials [1]. Since core level absorption is generally isolated in energy from other rapidly varying features, it can be useful in studying atoms present in low concentration. Thus XANES is a powerful tool for studying impurities, and complex structures such as dispersed catalyst particles. The advent of high-brightness polarized synchrotron x-ray sources has provided experimental opportunities not previously available, and a stimulus for detailed theoretical analysis.

Characterization of catalytic elements in operating environments presents an important opportunity for gaining greater insight into both the electronic and structural properties of the species actually present during operation. While EXAFS is normally considered the best atom-centred structural probe of such systems, the operating constraints of catalysts often pose limitations on the usefulness of EXAFS. For example, high temperatures, heterogeneous solution environments, rapid ligand exchange, or an inhomogeneous environment may limit the number of useful EXAFS data which can be collected or render interpretation of such data particularly troublesome. Further, electronic information is not available from the extended fine structure, but it is embedded in the bound to bound and resonance excitations near the absorption threshold. While some information can be extracted through analogy with known reference compounds, detailed information about electronic and structural properties really must be obtained from computations based upon suitable model and trial structures. Only in this fashion can distinctions between backscattering resonances and electronic excitation be made.

Near-edge features are sufficiently complex so that detailed theoretical modelling is required to obtain useful interpretations of the copious data which can be measured. In

this paper, calculations of the L_1 and $L_{2,3}$ cross-sections of rhodium in RhCl$_3$, Rh$_2$O$_3$, and [Rh(CO)$_2$Cl]$_2$ are reported and compared with experiment. Rh is formally trivalent in the chloride and oxide, and monovalent in the carbonyl; the environment is sufficiently different to result in significant electronic structure variations at the metal sites. These variations in metal configuration, and the backscattering of photoelectrons from neighbouring sites are the subject of our present interest. With a good understanding of Rh L edge features in these compounds, more complex systems hopefully can be described by analogy.

In recent years many theoretical and experimental studies of fundamental aspects of XANES and its use as a structural tool have been reported [2]. Here, a summary of the main features used in the present work is given. The x-ray absorption spectrum, due to excitation of a core level, is described in the dipole approximation by [3, 4]

$$\mu_i(E) = (4\pi^2)\alpha h\nu \sum_f |\langle \psi_f|\hat{e} \cdot r|\phi_i\rangle|^2 \, \delta(h\nu - E_f + E_i) \tag{1}$$

where $\alpha = e^2/\hbar c$ and $\hat{e}$ is the polarization vector of the incident radiation of frequency ν. The initial state ϕ_i is a simple atomic core state; useful information is found in the excitation energy and structure of the final state ψ_f. Two approaches are currently popular: (i) molecular cluster, and (ii) band structure formalism. The former is particularly applicable where ψ_f is taken to be a solution for the localized non-periodic excited atom potential [5]. The cluster-model or band-model ψ_f must include local on-site effects, single backscattering from neighbouring atoms, the spatial variation of the scattered wavelets, and, at low energies, multiple-scattering effects. Unlike the cluster approach, the band structure formalism is restricted to a periodic potential. The advantageous feature of both band structure and cluster multiple-scattering approaches is that they include multiple scattering to infinite order. This is in contrast to the single-scattering approach adequate for energies well above threshold, and used in the extended x-ray absorption fine structure (EXAFS) approach [6]. XANES can profitably be discussed both in terms of orbital hybridization and spectral density of states. Müller [7] has reconciled these two viewpoints, using the band formalism. The white line (WL) near the edge, a spectacular feature of on-site dipole-allowed transitions, can be understood in terms of peaks in the unoccupied portion of the densities of states. Equally well, the cluster approach allows an interpretation in terms of atomic resonances, perturbed by the mixing (hybridization) of on-site components of ψ_f with neighbouring sites.

Rh presents an interesting challenge for the use of both experimental and computational techniques for obtaining and analysing XANES data. Rh has been proposed to form several poorly defined structures on catalyst supports in response to various operating environments. For example, when deposited on γ-alumina and exposed to high-temperature oxidizing conditions, it has been suggested that Rh may dissolve into the alumina lattice. Recently, EXAFS measurements have confirmed an oxidized Rh environment in such catalysts consistent with Rh in an Al site within the support oxide. While EXAFS provides information about the radial distribution of neighbouring shells, greater structural insight might be gained from a detailed correlation between the Rh L edge XANES features and proposed models of such a Rh 'spinel'-like site. Similarly, exposure of highly dispersed Rh clusters on alumina to CO results in the formation of geminal dicarbonyl species with a formal oxidation state proposed to be $+1$. EXAFS analysis of such catalysts reveals a loss of Rh–Rh coordination, suggesting complete disruption of the small, metallic Rh clusters initially present [8] . However, absence of Rh–Rh correlation could equally well be related to an extremely disordered structure where the ensuing Rh–Rh pair correlation becomes sufficiently broad so as to render an EXAFS peak unobservable. An independent measure of the exact Rh

environment would help to further elucidate the chemistry taking place in this system. In the present calculations, we find that off-site Rh 4f resonances contribute importantly to observable features 18–40 eV above threshold. This 4f resonance apparently has not been remarked previously; it can give important information about the metal particle geometry and composition. Finally, we suggest that the joint application of theoretical modelling and accurate measurement of XANES at the Rh L_1 edge has the potential to offer information complementary to that from $L_{2,3}$ data.

2. Cluster models of rhodium compounds

The cluster multiple-scattering (MS) method [9] has been used in the XANES calculation of the compounds $RhCl_3$, Rh_2O_3, and $[Rh(CO)_2Cl]_2$. The cluster size chosen is a compromise between the desire to represent the crystalline or molecular environment adequately, and the need to control computation time. Merits and deficiencies of the multiple-scattering approach, as conventionally used with a 'muffin tin'(MT) approximation to the potential, have been adequately discussed [10]. Here we merely list the main computational parameters, and describe clusters selected for study.

2.1. Rhodium sesquioxide

Rh_2O_3 is an insulating grey or grey–black crystal. It has corundum structure [11], from which a 32-atom cluster centred on a Rh atom was generated. The cluster has 14 rhodium and 18 oxygen atoms as shown in figure 1(a), belonging to the C_3 symmetry group with a and e representations. According to the dipole selection rule, the L_1 edge is due to transitions from the 2s core state to both a and e final states, and the $L_{2,3}$ edge is due to transitions from $2p_{1/2}$ and $2p_{3/2}$ levels to a and e. The central Rh atom is chosen as the excitation site, with atomic sphere radii (R), and maximum orbital angular momentum (L_{max}), included in the MS expansion as given in table 1.

2.2. Rhodium trichloride

The structure of $RhCl_3$ is of $AlCl_3$ type ($CrCl_3$ with pseudohexagonal layer lattice) [12]. The 16-atom idealized cluster, which is slightly deformed from the real structure (see figure 1(b)) used here includes four rhodium and 12 chlorine atoms. This cluster also has C_3 symmetry, having a and e representations, with excitations generated at the central Rh atom.

2.3. Rhodium dicarbonyl chloride dimer

The rhodium dicarbonyl chloride dimer compound $[Rh(CO)_2Cl]_2$ exists as a molecular crystal, figure 1(c), whose synthesis and characterization were given by Dahl *et al* [13]. It is orange–red and has unusual booklike structure with a Rh–Rh Cl bridge; some evidence was claimed for a metal–metal bond. This compound is a catalyst for strained hydrocarbon rearrangements and olefin hydroformylation. The isolated molecule of C_{2v} symmetry, with a_1, a_2, b_1, and b_2 representations, has been chosen for study since the inter–molecular interaction is expected to be relatively weak. In this case, we are primarily interested in effects of bridging Cl and CO terminal ligands on the Rh L cross-section.
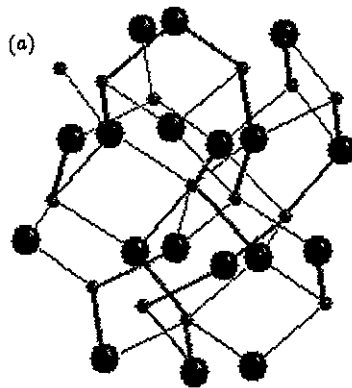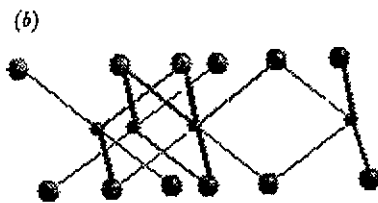
Fig. 1(a)

Fig. 1(b)

Fig. 1(c)

Figure 1. Clusters used in calculations. (a) $Rh_{14}O_{18}$ cluster for Rh_2O_3; large balls are oxygen, (b) Rh_4Cl_{12} cluster for $RhCl_3$, large balls are chlorine; and (c) $[Rh(CO)_2Cl]_2$ molecule, two central large balls are bridging chlorine, small balls are rhodium, and CO are attached to Rh.

Table 1. Muffin tin parameters used in MS cross-section calculations.

Clusters	R^a (Å)					L_{max}^b				
	os^c	Rh	Cl	O	C	os	Rh	Cl	O	C
$Rh_{14}O_{18}$	5.19	1.07		1.07		12	4		3	
Rh_4Cl_{12}	6.13	1.32	1.32			12	4	3		
$(Rh(CO)_2Cl)_2$	5.34	1.17	1.32	0.95	0.90	12	4	4	3	3

[a] R is radius of each atomic volume and outer sphere.
[b] L_{max} is maximum value of angular momentum in partial wave expansion of ψ_f.
[c] os denotes outer sphere surrounding cluster.

3. Edge structures and potentials

3.1. L_1 Edge

The experimental L_1(2s) threshold in the metal is 3.412 keV; by the dipole selection rule, the cross-section should be dominated by Rh 2s → p transitions. The Rh 4p state is fully

occupied, while 5p is empty and possibly lying in the continuum region with position depending upon the valence state. A sharp linelike absorption, or 'white line' (WL), is often observed in the initial absorption rise at the edge of a semiconductor, an insulator, or a semimetal, and can arise if there are unoccupied electronic states of the required symmetry with a high density of states at the absorption edge [15]. Since the L_1 spectra have not been reported we can make a prediction: we show below that the 5p resonance is sufficiently narrow to produce a WL, centred about 5 eV above the edge in oxide and carbonyl and 2 eV in chloride. Since this intense feature is chemically sensitive, we suggest that L_1 contains sufficient information, not subject to the same selection rules as $L_{2,3}$, to make experimental studies worthwhile.

3.2. L_2 and L_3 Edges

In experiment, $L_2(2p_{1/2})$ and $L_3(2p_{3/2})$ edges, which are at 3.146 and 3.003 keV respectively in metallic Rh, are well separated, as the two initial states are split by approximately 142.3 eV [14] spin–orbit coupling. In $L_{2,3}$ edges of transition elements, there should be a strong WL, where there is a high density of empty d states. The s final states are usually unimportant for the WL [16], since the s band is quite broad. Sham [15] finds that a WL is present in Pd $L_{2,3}$ absorption, but not in Ag $L_{2,3}$, consistent with the high density of unoccupied Pd d states around the Fermi energy while $Ag(d^{10})$ has none. Sham [18] also points out that there are WL in both L_2 and L_3 absorption in metallic Rh. The ground configuration of Rh is $[Kr](4d_{3/2})^4(4d_{5/2})^4(5s_{1/2})^1$; i.e. the $j = \frac{3}{2}$ d subshell is completely full. On this basis one might expect to see *no* WL for L_2 $2p_{1/2} \rightarrow 4d_{3/2}$ allowed transitions, and $p_{1/2} \rightarrow d_{5/2}$ is dipole forbidden ($\Delta j = \pm 1$, 0; no $0 \rightarrow 0$). However, in transition metals, 5s, 5p, and 4d hybridization pushes some $d_{3/2}$ states above the Fermi energy and some p $\rightarrow$ d intensity appears in L_2. In Rh_2O_3 we have the nominal Rh^{3+}, $(4d_{3/2})^4(4d_{5/2})^2(5s_{1/2})^0$ configuration, with a calculated $d_{3/2}$–$d_{5/2}$ spin–orbit splitting of 0.4 eV. Again we may ask about the possibility of finding $d_{3/2}$ holes in the compounds, leading to observable WL features in L_2 spectra. We find, in the three compounds studied here, the metal–ligand interaction leads to bonding/antibonding interactions which are considerably stronger (1–3 eV) than the spin–orbit splittings. Thus, for reasons similar to those for the metal, the L_2 and L_3 spectra are similar in appearance. This is fortunate since the non-relativistic MS method used here cannot directly find the shape difference between L_2 and L_3 edges. Sub-cross-sections, for p $\rightarrow$ s and p $\rightarrow$ d transitions, weighted according to the selection rules and degeneracy, have been formed for comparison with experiment. We will show that the p $\rightarrow$ d oscillator strength contributes mostly to the near-edge and pre-edge region, while p $\rightarrow$ s transitions appear dominant in the higher-energy backscattering region.

3.3. Effective potentials

Neutral, ionic and self-consistent field atomic configurations were used here to span the range of plausible potentials, using the local density (LD) theory [19]. Thus three different potentials were used to calculate L_1 and $L_{2,3}$ edges, in order to explore the sensitivity of cross-section to atomic configuration. The neutral configurations and 'fully ionic' states of the component atoms are given in table 2. More accurate first-principle models of charge and potential distributions were obtained by treating embedded clusters, using the self-consistent field DV-X_α method [20]. Details of these calculations will be published elsewhere. Here, the effective atomic configurations obtained by Mulliken orbital population analysis of cluster wavefunctions are summarized in table 2.

Table 2. SCF atomic configurations found by embedded cluster method, and neutral atomic and fully ionic configurations.

Compound	Cluster	Rh	Cl	O	C
Rh_2O_3	$Rh_{14}O_{18}$	4d 6.63		2s 1.94	
		5s 0.05		2p 5.51	
		5p 0.14		3s 0.00	
	Net charge	+ 2.18		−1.45	
$RhCl_3$	Rh_4Cl_{12}	4d 6.93	3s 1.98		
		5s 0.17	3p 5.44		
		5p 0.09	3d 0.19		
	Net charge	+ 1.81	−0.60		
$[Rh(CO)_2Cl]_2$	$(Rh(CO)_2Cl)_2$	4d 7.51	3s 2.00	2s 1.99	2s 1.96
		5s 0.47	3p 5.56	2p 4.19	2p 1.99
		5p 0.11	3d 0.03	3s 0.01	3s 0.00
	Net charge	+ 0.91	−0.59	−0.19	+ 0.04
Neutral atoms		$[Kr]4d^8 5s^1$	$[Ne]3s^2 3p^5$	$1s^2 2s^2 2p^4$	$1s^2 2s^2 2p^2$
		$5p^0$	$4s^0$	$3s^0$	$3s^0$
Fully ionic		$[Kr]4d^6 5s^0$	$[Ne]3s^2 3p^6$	$1s^2 2s^2 2p^6$	$1s^2 2s^2 2p^1$
		$5p^0(+3)$	$4s^0(-1)$	$3s^0(-2)$	$3s^0(+1)$

For Rh_2O_3 and $RhCl_3$, the clusters were embedded in the infinite crystal [21]; an isolated molecule was used in the $[Rh(CO)_2Cl]_2$ case. In every case a muffin tin (MT) approximation to the DV-X_α potential was constructed for use by the MS procedure to calculate ψ_f. The MT potential was formed by spherically averaging charge density and Coulomb potential inside each atomic sphere. A volume average was formed for the interstitial region. The potential in the outer sphere (OS) region was constructed by making a smooth transition from the interstitial value to that of a shell of charge $+e$ located at the OS surface, representing a delocalized core hole final state distribution. The OS potential has the form

$$V(r) = \begin{cases} -(Q/r)\exp[-((r - R_{OS})/d)] & R_{OS} \leqslant r \leqslant R \\ -1/r & r > R. \end{cases} \qquad (2)$$

Here, $R = R_{OS} + d \ln Q$, d has been chosen to be 1.06 Å and Q is determined by matching $V(R_{OS})$ to the constant potential in the interstitial region.This OS potential establishes boundary conditions for the Coulomb wave which matches onto the cluster wavefunction at the outer sphere radius. Physically it models a 'relaxed average' core hole distributed over the cluster. This model has been found to give relative energy positions and amplitudes reasonably well. When more precise results are required in a particular energy region, transition state calculations, which explicitly treat the energy-dependent core relaxation, can be made [22].

4. Results

4.1. Experimental features

Sample preparation and measurements were carried out by H J Robota of Allied Signal Corp., as detailed in the appendix. Experimentally, the L_3 XANES portion of the spectrum

shown in figure 2 differs among the materials, but the differences are not sufficient to allow easy interpretation of unknown structures. Elucidation of unknowns would require the availability of a sizable database of reference spectra obtained from a wide variety of known compounds with known structures. Large differences are observed in the white line intensity. Surprisingly, the white line of $[Rh(CO)_2Cl]_2$ is substantially stronger than observed from Rh_2O_3, the integrated WL intensity being in the ratio $Rh_2O_3(0.8) < RhCl_3(1) < [Rh(CO)_2Cl]_2(1.3)$. Since the more ionic Rh_2O_3 has more 4d hole states than $[Rh(CO)_2Cl]_2$ Rh, exactly the opposite would have been expected. The nominal charge differences (Rh^{3+} against Rh^+) are borne out by the computated Mulliken charges, $Rh_2O_3(2.2) > RhCl_3(1.8) > [Rh(CO)_2Cl]_2(0.9)$, so that it becomes clear that the WL intensity is not simply correlated to the Rh charge, or even the net 4d occupation. In the following we analyse the final state content in more detail, to obtain a better understanding of the spectral features. The most obvious features lying well above the WL are listed in table 3. Because of lack of purity of the $[RhCl(CO)_2]_2$ material and other possible technical problems, the measured spectra show no obvious distinct peaks above the WL in the L_3 spectra.

Table 3. Main features of the experimental L_3 edge well above the white line. Peak positions are given with respect to the white line.

Peak	Position (eV)	Peak relative intensity	Width (eV)
Rh_2O_3			
B	20.0	0.02	7.0
	28.0	0.05	5.0
C	45.0	0.24	17.0
D	113.0	0.24	18.0
$RhCl_3$			
B	13.0	0.06	7.0
C	49.0	0.24	18.0
D	102.0	0.07	22.0

4.2. Possible experimental test of 4f resonance structure correlation

A very interesting aspect of the computational results relates to Rh–Rh f orbital resonances observed at energies well above threshold, and discussed in detail below. This feature may well prove valuable in characterizing operating catalyst systems; it should be possible to explore this feature further in a straight forward experimental measurement. Well dispersed, supported Rh catalysts can be prepared with Rh loadings adequate for high-quality measurements of the L_3 edge features. By varying the preparative conditions, particles of widely varying sizes can be produced, from particles containing only a few atoms to those with diameter of the order of 100 Å. Considerable EXAFS evidence has been gathered indicating that the smallest, bare particles have Rh–Rh bond lengths substantially shorter than those found in either much larger particles or bulk metal. This contraction of the interatomic distance can be relaxed through the absorption of H. By preparing a series of samples with differing particle size initially and comparing both bare and H-covered particles, two different, interleaving data sets of variable Rh–Rh interatomic distances could be gathered [8]. Further, conventional Rh L edge EXAFS can be used to verify the bond lengths under each of these conditions. Should the value of these f resonances be confirmed using well defined materials, further experimental support could be obtained by examining
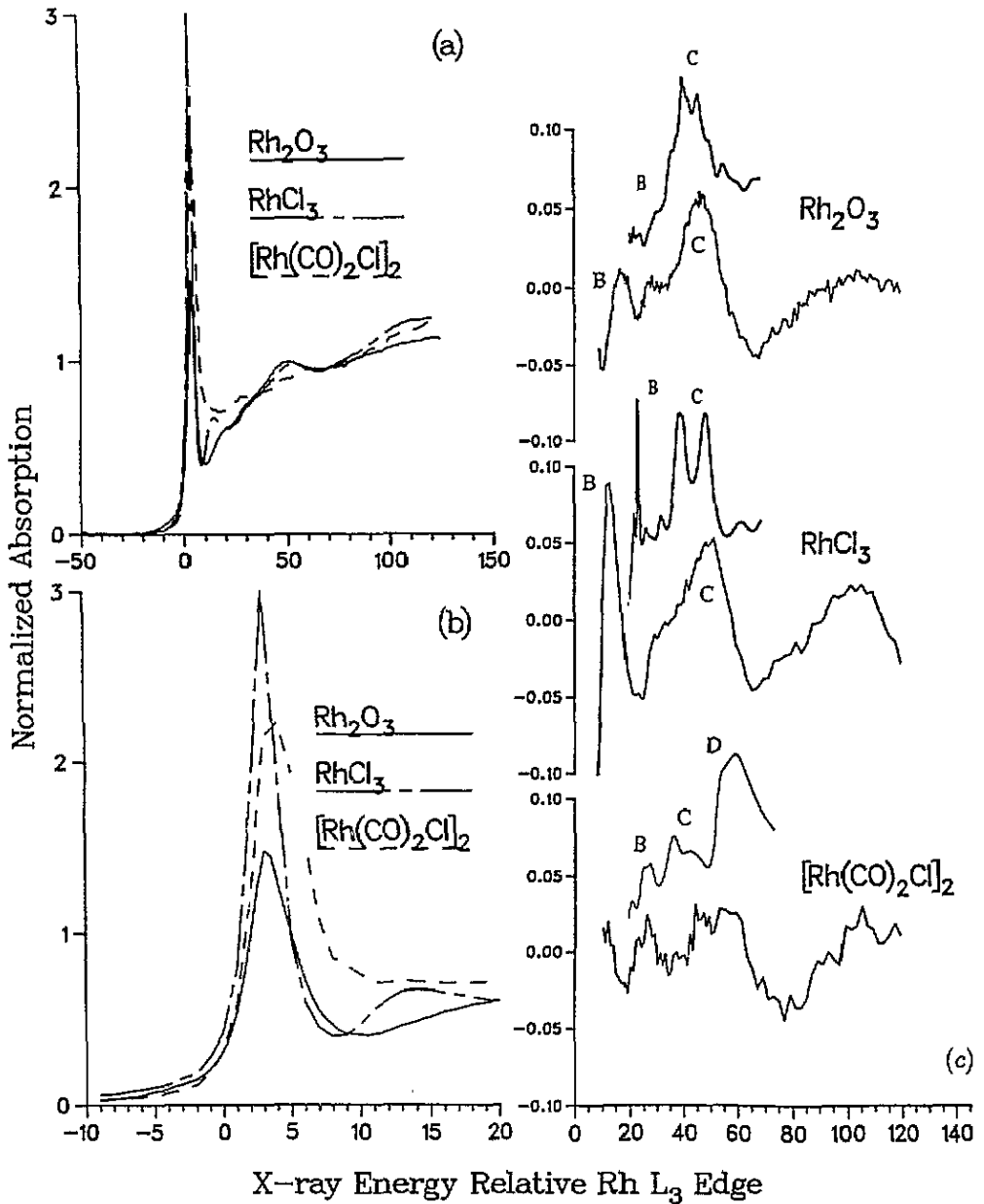
Figure 2. Experimental L_3 edge spectra of RhCl$_3$, Rh$_2$O$_3$ and (Rh(CO)$_2$Cl)$_2$ (a) normalized absorption, (b) the 'white lines', and (c) structures to higher energy, each comparing with the calculated counterpart. The zero energy for both theory and experiment is set to the continuum edge.

the influence of CO exposure. As noted in the introduction, very small Rh particles, when supported on γ-Al$_2$O$_3$, appear to undergo complete disruption while larger particles may undergo only partial disruption. The intensity and energy position of the f resonances may prove diagnostic under these conditions.

4.3. Detailed analysis

4.3.1. Rh_2O_3.

The L_1 absorption into a and e symmetry final states is shown in figure 3, along with the total cross-section. The s $\rightarrow$ p selection rules here probe a different portion of the final state structure than do $L_{2,3}$. Detailed features, which we now discuss, suggest that it is worthwhile to experimentally analyse this region, if experimental difficulties mentioned above can be overcome. Neutral atomic, ionic, and SCF potentials produce qualitatively similar cross-sections. The main features are identified and compared in table 4, where the final state analysis given is defined by integrated $|\psi_f|^2$ components of specified angular momentum within each atomic sphere. We present relative values here; a more extensive discussion in terms of photoelectron 'trapping times' is given by Guo *et al* [22]. The observed absorption intensity is of course due to the Rh_1 p component here; knowledge of the composition of remaining components of ψ_f is essential to use of XANES as a chemical tool.
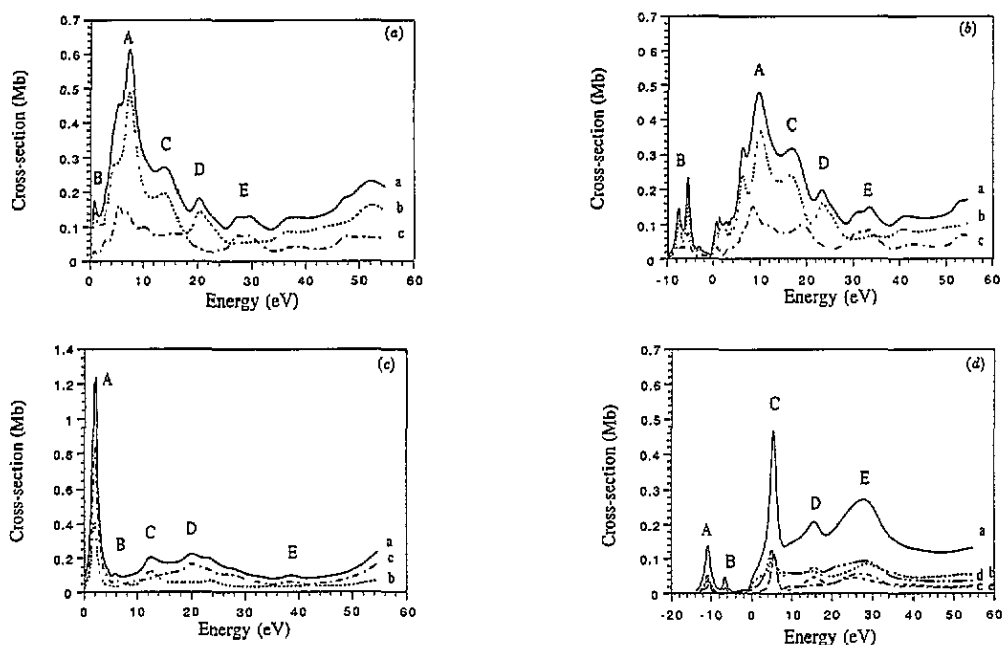

Figure 3. Calculated L_1 edges in SCF potential. (a) Rh_2O_3, solid line total cross-section; dotted line, scattered into a, and dashed line, into e, final states; (b) Rh_2O_3 with 5% bond length contraction; (c) $RhCl_3$, with same labelling as (a); and (d) $(Rh(CO)_2Cl)_2$, solid, total cross-section; dotted, scattered into a_1; dashed–dotted, scattered into a_2; dashed–triple dotted, scattered into b_1, and dashed, scattered into b_2. The continuum onset is at *zero* energy.

There are only very small peaks below threshold (hardly to be seen); i.e., bound to bound state transitions are not significant. This also can be predicted by viewing the densities of states discussed below. There are no empty Rh p orbitals below E_F; the 4p is fully occupied, and the '5p' resonance has not yet appeared. This is in agreement with Sham's conclusion on metallic Rh and Pd mentioned before that there is no WL at or below the L_1 edge. The small peaks, B, in Rh_2O_3 are due to p orbital admixture of surrounding oxygen atoms, an evidence of covalency in this material. Table 2 shows that there are about $0.5e$ holes per oxygen atom in its 2p shell, which are responsible for these features. The

Table 4. Main features of L_1 edge in different model potentials. Peak positions are given with respect to continuum edge.

Peak	Peak position (eV)				Contribution of selected atomic orbitals (%) to final states in SCF model potential; s, p, d, and f refer to angular momentum			
	Neutral	SCF	SCF 5% bond contraction	Ionic	Rh	O	Cl	C
Rh$_2$O$_3$								
B	1.0	1.0	−8.0 −6.0	1.5		O$_6$[a] p 9		
A	7.0	7.5	9.5	10.0	Rh$_1$ p 5	O$_2$ d 9		
C	14.0	13.5	10.7	15.0	Rh$_1$[b] f 3 Rh$_s$ f 19	O p 19		
D	20.0	20.0	23.5	21.0	Rh$_s$ f 39			
E	28.0	29.0	33.5	31.0	Rh$_1$ f 3 Rh$_s$ f 46			
RhCl$_3$								
A	5.7	2.5		−0.6	Rh$_1$ p 11		Cl$_1$ d 45	
B	9.2	5.7		4.0			Cl$_1$ d 52 Cl$_2$ d 30	
C	16.5	12.2		9.9	Rh$_1$ p 3		Cl$_1$ d 20 Cl$_2$ d 30	
D	22.0	20.0		13.5 17.6	Rh$_2$ f 20		Cl$_1$ d 11 Cl$_2$ d 17	
E	30.5	39.0		31.7	Rh$_2$ f 9		Cl$_1$ f 16 Cl$_2$ p 17	
(Rh(CO)$_2$Cl)$_2$								
A	−4.7	−10.5		−11.0	Rh$_2$ d 30		Cl p 42	
B		−6.5			Rh$_2$ d 11	O p 11	Cl p 41	
C	6.6	6.3		−7.2	Rh$_1$ p 11		Cl d 28	C d 17
D	17.0	15.5		2.0	Rh$_1$ p 6 Rh$_2$ f 7	O d 17	Cl d 11	C d 23
E	30.0	28.0		12.0	Rh$_2$ f 21	O d 12		C d 14

[a] O_x and Cl_x: $x = 1$ nearest to Rh_1; $x = 2$ next nearest.

[b] Rh_x: $x = 1$ absorbing atom; $x = s$ surrounding Rh atoms and $x = 2$ next-nearest atoms.

main peak just above the continuum threshold, A, is due to rhodium '5p' final states. The doublet substructure is evidence of bonding (lower energy) and antibonding (upper energy) interaction between Rh 5p and oxygen ligands. At an energy of ~14.0 eV, peak C, the surrounding rhodium atoms f orbital resonance first appears with noticeable intensity. We will see a similar situation in the other compounds, and in higher-energy features of the $L_{2,3}$ XANES of Rh$_2$O$_3$. The small Rh_1 f orbital weight in peaks C and E is caused by hybridization of s, p, d, f, ... states in C_3 symmetry.

A detailed comparison of neutral, ionic, and SCF potential results shows that the major peaks keep a relatively similar shape, with the SCF potential producing a cross-section intermediate between those of ionic and neutral potentials. Examination of table 4 shows that the neutral atom configuration produces an L_1 spectrum with peak positions and atomic composition rather similar to those of the SCF potential. Thus atomic, rather than ionic configurations may provide a 'best guess' when SCF is not available. The SCF calculation for Rh$_2$O$_3$ with 5% reduction in bond lengths relative to experiment shows the high sensitivity of observable features to these geometrical parameters.

Table 5. Main features of the $L_{2,3}$-edge in different model potentials, given with respect to the continuum edge; Rh_1 refers to the excited atom; Rh_2 are the nearest neighbours and Rh_3 are the next nearest neighbours, and so on. O are nearest oxygen atoms, O_2 are the next nearest oxygen atoms.

Peak	Peak position (eV)				Contribution of selected atomic orbitals to final states in SCF model potential; s, p, d, and f refer to angular momentum			
	Neutral	SCF	SCF 5% bond contraction	Ionic	Rh	O	Cl	C
Rh_2O_3								
A	−5.0	−2.0	−5.0	−8.0	Rh_1 d 22			
		−5.0	−2.5	−5.5	Rh_1 d 9	O p 58		
			−1.0	−1.0				
B	1.0	3.0	4.0	2.0	Rh_1 s 2	O_2 d 7		
					Rh_2 s 2	O_6 p 7		
					Rh_6 p 3			
C	34.0	24.0	31.0	29.0	Rh_4 f 20			
$RhCl_3$								
A	−6.0	−16.0		−27.0	Rh_1 d 53			
					Rh_s d 27			
	−4.0	−10.0		−23.0	Rh_1 d 19		Cl_1 p 11	
B	7.2	4.0		−12.0	Rh_2 p 3		Cl_1 d 51	
							Cl_2d 20	
C	25.7	22.0		∼2.5	Rh_1 f 2			
					Rh_2 f 30			
D	38.8	32.0		17.0	Rh_2 f 13		Cl_1 f 16	
							Cl_2 d 15	
$(Rh(CO)_2Cl)_2$								
A	−6.5	−12.0			Rh_1 d 68		Cl p 11	
	−4.5	−7.5			Rh_1 d 36		Cl p 27	
B	9.5	∼8.0			Rh_1 d 8	O d 12	Cl d 44	C p 14
C	19.0	−18.5			Rh_2 f 11	O d 9	Cl d 11	C d 26
							Cl f 9	
D	42.0	∼40.0		10.05	Rh_1 d 11		Cl f 16	
					Rh_2 f 9		Cl d 9	C d 16
E				26.3	Rh d		Cl f	

Cross-sections of the calculated $L_{2,3}$ absorption are presented in figure 4, which are comparable to experiment; the main features are analysed in table 5. In $L_{2,3}$, we expect strong p → d bound to bound transition peaks just below the edge. By analysing the final state wavefunctions, these peaks are verified to be indeed of Rh 4d character. The abrupt jump in $\mu(E)$ at $E = 0$ is an artifact of the MS scheme which could be avoided by shifting the potential 'floor' to effectively raise the empty d levels into the continuum. Since the MT potential approximation used in MS calculations introduces some uncertainty in composition and position of bound states, analysis of this region by use of DV-X_α wavefunctions also has been performed. Here, it is convenient to introduce the *projected* density of states (PDOS)

$$N_p(\varepsilon) = \sum_i n_{ip} L(\varepsilon - \varepsilon_i, \gamma) \tag{3}$$

where $n_{ip} = |C_{ip}|^2$ is the diagonal density component of atomic orbital p in cluster wavefunction i, and L is a Lorenztian line-shape function with half-width γ. The coefficients C_{ip} define the variational expansion of cluster orbitals ψ_i in terms of symmetrized atomic

orbitals χ_p:

$$\psi_i = \sum_p \chi_p C_{ip}. \tag{4}$$

The PDOS is useful here in selecting final state components which satisfy transition selection rules, and should not be confused with *partial* densities of states which include hybridization terms. The DV projected densities of states show, in figure 5, that the Rh 4d band is relatively narrow (~5 eV) with a sharp peak just above E_F. There is negligible Rh s and p character in this region.

In contrast to the L_1 edge, we find $L_{2,3}$ structure is rather sensitive to atomic configuration, although similar features are seen in each case. The small features in Rh_2O_3 around B (see table 5), just 2–3 eV above threshold, are backscattering mainly from the nearest oxygen p orbitals. The major broad resonance around ~20–30 eV above the edge centred on peak C has a major contribution from surrounding rhodium atom f orbitals. This 4f resonance could be expected to appear due to the semilocalized nature of $l = 3$ states and was identified above in the L_1 spectra. This feature appears weak in comparison with the p $\rightarrow$ d WL structure; however, it should be easy to detect against the smooth background. We find this to be a pervasive feature, which however, does not seem to have been commented upon previously. Since it is a result of metal–metal interaction, it is potentially very useful as a measure of the Rh–Rh structural parameters in a complex system, including alloyed and oxidized particles. At higher energy mixing features appear due to surrounding Rh high-energy empty d orbitals and other states, marking the onset of the EXAFS region.

Figures 3(b) and 4(b) give the L_1 and $L_{2,3}$ absorption of Rh_2O_3 with all interatomic distances reduced to 95% of the experimental bond length. The major features are similar to those found with the equilibrium bond length; however, interpretation of differences allows us to estimate the value of these features as a structural diagnostic. The major peaks keep relative positions and intensities similar to those for the equilibrium bond length, but broaden slightly which can be attributed to increased Rh–O interaction. The L_1 edge is less sensitive to the geometrical parameters, compared to $L_{2,3}$. For example, the $L_{2,3}$ WL is broadened, from ~6 eV to ~10 eV due to the broader 4d state distribution at shorter bond length, caused by increased Rh d–O p mixing. The Rh 4f resonance, peak C, has been pushed up to higher energy by 7.0 eV; thus a measure of structural sensitivity of this feature is $(\delta E/E)/\delta R = 1.79$ Å^{-1}, where R is the Rh–Rh distance. Very simple scattering models would lead one to expect $kR \simeq$ constant, where $k = \sqrt{E}$, and some scattering peaks do indeed behave in this fashion. However, bonding considerations lead to more complex behaviour in molecules [17], and also in solids.

4.3.2. RhCl₃. The calculated L_1 edge of $RhCl_3$, given in figure 3(c), shows some important differences, compared to that of Rh_2O_3. The main peaks fall at lower energy here, and the '5p resonance' is much sharper. In the ionic potential model, it is also notable that the main peak is found -0.6 eV below the continuum threshold. The backscattering resonance peaks due to the surrounding Rh f orbitals are of relatively smaller intensity and lower energy than the oxide, occuring around 20–39 eV. All of these feature are consistent with weaker interatomic interactions in the chloride compared to the oxide. The L_1 features assignment is given in table 4.

The calculated $L_{2,3}$ edge spectra for $RhCl_3$ are given in figure 4(c); the analysis of the main features is given in table 5. We note that the muffin tin averaging of this rather anisotropic system has pushed the p $\rightarrow$ d transitions unrealistically low, compared to the
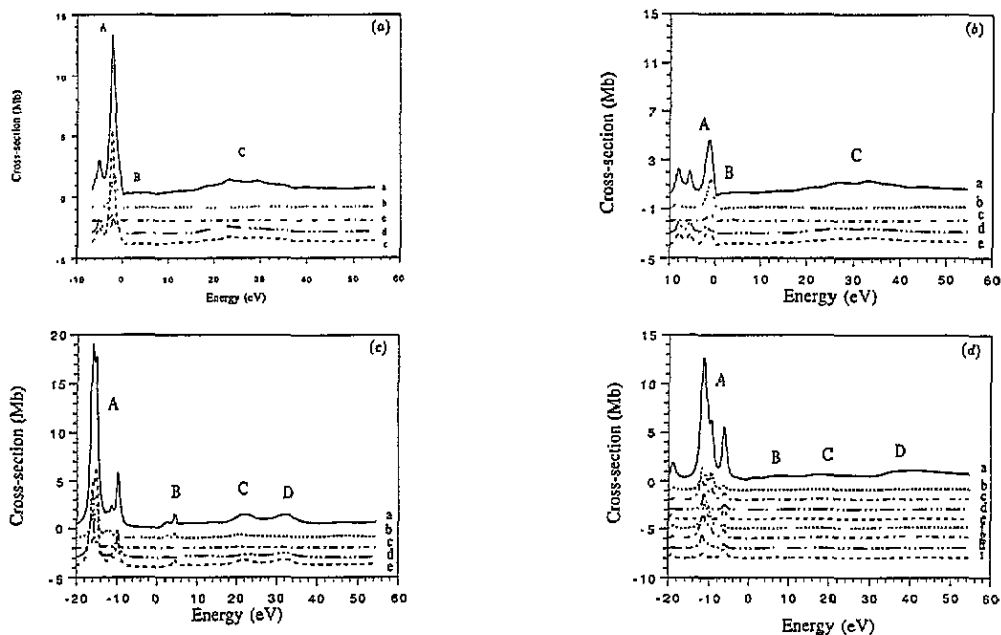
Figure 4. Calculated $L_{2,3}$ edges in SCF potential. (a)Rh$_2$O$_3$, solid, total cross-section; dotted, scattered into a from $2p_z$, dashed–dotted, scattered into a from $2p_{xy}$; dashed–triple dotted, scattered into e from $2p_z$; and dashed, scattered into e from $2p_{xy}$; (b) Rh$_2$O$_3$ with 5% bond length; (c) RhCl$_3$, with same labelling as (a); and (d) (Rh(CO)$_2$Cl)$_2$, solid, total cross-section; upper part: dotted, scattered into a$_1$ from $2p_z$; dashed–dotted, scattered into a$_1$ from $2p_{xy}$; dashed–triple dotted, scattered into a$_2$ from $2p_z$; dashed, scattered into a$_2$ from $2p_{xy}$; lower part: dotted, scattered into b$_1$ from $2p_z$; dashed–dotted, scattered into b$_1$ from $2p_{xy}$; dashed–triple dotted, scattered into b$_2$ from $2p_z$; and dashed, scattered into b$_2$ from $2p_{xy}$. The continuum onset is also at *zero* energy.

continuum edge. The main features are probably correctly determined, aside from an energy shift.

The projected densities of states of RhCl$_3$ are given in figure 5(b). Although we have argued that the Rh–Cl interaction is weaker than that of Rh–O, resulting in lesser charge transfer, we see that the Rh 4d band actually broader here, $\sim$10 eV in width. This is due to a 'covalent tail' extending over the Cl 3p valence band. As the number of 4d 'holes' in RhCl$_3$ is 0.3e less than in Rh$_2$O$_3$ (see table 2), the integrated intensity of the WL in RhCl$_3$ might have been expected to be weaker than in Rh$_2$O$_3$. Sayers and others have used integrated intensities to try to put WL analysis onto a quantitative basis [6]. However, differing degrees of covalency and charge transfer in the final states cause the absorption to be distributed in a more complex way than can be represented simply by counting d holes. In the energy range 20–40 eV, the calculated $L_{2,3}$ edge displays f resonance peaks (C, D) caused by back scattering from the neighbouring Rh atoms, as in Rh$_2$O$_3$.

4.3.3. [RhCl(CO)$_2$]$_2$. The calculated L$_1$ edge cross-section is shown in figure 3(d) and the composition of the major features is given in table 4. The main peak C, at 6.3 eV above threshold, is largely contributed by the bridging chlorine d orbitals and also has some excited rhodium p and carbon d contribution. Two smaller peaks below the threshold, A and B, are mainly caused by Cl p and C p scattering respectively. The broad peaks above the
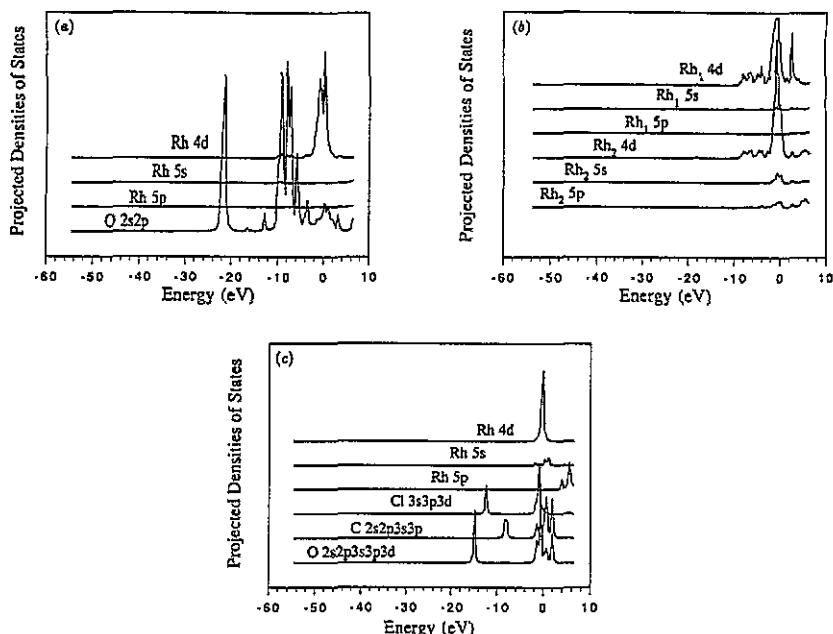
Figure 5. Projected densities of states (in arbitrary units). (a) Rh_2O_3: O 2s2p, Rh 5p, Rh 5sv, and Rh 4d calculated by DV-X_α SCF method, in ground state. The baseline of each curve is offset by 10 units for easy readability. (b) $RhCl_3$: Rh_1 is the central Rh atom and Rh_s the surrounding Rh. (c) $(Rh(CO)_2Cl)_2$. The Fermi energy is marked as zero.

threshold, D (~ 16 eV) and E (~ 28 eV), contain the neighbouring Rh f character common to all of the compounds studied here. We also found the calculated L_1 edge in SCF and neutral atomic configuration potentials to be very similar both in shape and peak positions, while the ionic configuration is grossly in error.

The calculated $L_{2,3}$ edge of the carbonyl chloride compound (see figure 4(d)) shows a backscattering structure much weaker than in the oxide and chloride. Also, the positions and amplitudes are found to be sensitive to the geometric parameters of the MT potentials. The bridging chlorine d orbitals play an important role in the backscattering above the absorption edge, as noted for L_1. The number of 4d 'holes' in this compound ($2.45e$) is $0.88e$ less than those in oxide and $0.58e$ less than in chloride, which would suggest a less intense WL. However, as noted previously, the experimental WL for this compound is quite intense. From the calculated $\mu(E)$ we estimate relative integrated intensities as Rh_2O_3:Rh_2Cl_3:$[Rh(CO)_2Cl]_2 = 0.5:1:0.9$ (experimental 0.8:1:1.3), so our calculated white line for $[Rh(CO)_2Cl]_2$ remains in conflict with experiment. In view of the poorly resolved detail in the carbonyl compound, we suggest that further measurement would be useful.

The Rh 4d is also less hybridized and mixed with ligands, as can been seen from the calculated projected densities of states in figure 5(c), where the 4d character appears as a single, rather narrow (<3 eV) band. In table 5, we show the composition of main features of the $L_{2,3}$ spectrum. We found, in common with the other calculated $L_{2,3}$ edges, some small peaks above threshold which are related to neighbouring Rh f orbitals.

5. Discussion and conclusions

Experimental L_3 edge data for the three cases studied have principal features which are seen to be very similar to those calculated, except for some inevitable loss of detail. Features marked B, C and D in the preceding discussion can be identified with similarly labelled features of the experimental edges. The intense WL dominates the threshold region, and while no quantitative comparison is possible, we have made semiquantitative integrated intensity comparisons. The $RhCl_3$ peak is appreciably narrower than that of Rh_2O_3, in agreement with the calculations. The ligand backscattering peaks B and C are now clearly identified.

In table 6, the calculated Rh 4f resonance peak positions in different model systems are collected. In order to further demonstrate the generality of these phenomena, we include data for a tetrahedral Rh_4 particle, calculated using neutral atom configurations. The Rh_4 particle was calculated at the bulk intermetallic distance, and for a 10% reduction in bond length, to display structural sensitivity. Details of our analysis of Rh_n particle profiles will be given elsewhere; here we note the ubiquitous double-peak structure and its appearance in a well defined energy region.

Table 6. Calculated Rh–4f neighbour resonance peak positions.

Compounds	Rh–Rh distances (Å)	Peak positions (eV)
Rh_2O_3	2.71	23.0, 29.5
	2.57	27.0, 33.5
Rh_4	2.30	20.0, 42.0
	2.07	18.0, 38.0
$RhCl_3$	3.41	22.0, 32.0
$(Rh(CO)_2Cl)_2$	3.12	17.0, 40.0

The Rh 4f resonance is also quite noticeable in experiment, with those from the peak C of Rh_2O_3 and $RhCl_3$ being found at slightly higher energy than predicted in our calculations. We find that the experimental higher-energy peaks, D, are also related to neighbouring Rh f resonance. The carbonyl compound spectra suffer from a poor signal to noise ratio, which could be improved by optimizing sample absorbance. Those weak features seen correspond to the backscattering from the bridged chlorine and carbon around $8 \sim 40$ eV; f resonances are not resolved.

The density functional cluster approach has been used to study Rh L_1 and $L_{2,3}$ edges in three reference compounds of known crystal structure. Comparison of results for different model potentials reveals the sensitivity of L edge XANES to local atomic configuration, and gives a procedure for identifying those configurations in more complex environments. Observation of the prominent neighbouring atom Rh 4f resonance at $\sim$30 eV above threshold, with structural sensitivity $(\delta E/E)/\delta R = 1.79$ Å^{-1} in Rh_2O_3, provides a new means of studying Rh–Rh interactions which can be useful in interpreting metal particle structures.

Acknowledgments

Appendix. Sample preparation and measurements

At the low x-ray energy of the Rh L_3 absorption edge, care must be taken to prevent excessively thick samples in order to prevent distorting the intensities of the weak absorption features above the absorption threshold. As a result, powders of pure compounds are unsuitable as samples. In order to overcome this problem, samples were prepared on supports of either silica or carbon. All measurements were made on beamline X-19A of Brookhaven National Sychrotron Laboratory, using a two-crystal monochromator equipped with Si(111) crystals. Incident intensities were monitored using a He-filled ionization chamber connected to a He flow path where the samples were mounted. Fluorescence detection was used with a Stern–Heald detector filled with flowing nitrogen. The entire path between the exit from the I_0 detector and the sample and between the sample surface and the fluorescence detector window was continuously purged with a flow of He. Multiple data files were subsequently summed in order to improve the signal to noise ratio.

Measurements were only made at the L_3 x-ray absorption threshold for practical experimental reasons. When using fluorescence excitation detection, the L_3 edge is the lowest-energy L edge. Thus, contrast in the detection of fluorescence is highest in going from no fluorescence below the edge to a fluorescent signal proportional to the absorption cross-section as the edge is traversed. However, the Rh L edges are at closely spaced energies. Upon approaching the L_2 edge, strong fluorescent emission continues from excitation of atoms at the L_3 edge as well as new emission from atoms excited only at the L_2. Hence, interpretation of the signal becomes ambiguous. This compounding of fluorescent intensity continues into the L_1 edge as well, rendering the L_3 absorption edge the only practically available edge by fluorescence detection in this system. Due to the very strong absorption of x-rays at these low energies, preparation of pure samples sufficiently thin to permit transmission detection is practically prohibitive.

The Rh_2O_3 sample was prepared by impregnating Cab-O-Sil M5 fumed silica powder with a solution of aqueous $RhCl_3$ to incipient wetness. The Rh solution concentration was adjusted to produce a sample with a nominal Rh loading 5%. Following oven drying in air at 120 °C the sample was first reduced in flowing 5% H_2/N_2 at 800 °C and then oxidized in flowing air at the same temperature. X-ray diffraction analysis confirmed the presence of orthorhombic Rh_2O_3 with average crystallite size in the 500 Å range.

The $RhCl_3$ sample was prepared as a hydrated chloride. A portion of the sample used to prepare the Rh_2O_3 above was separated following the 120 °C oven drying. Again, XRD was used to confirm the presence of the crystalline, hydrous chloride.

Preparation of $Rh_2(CO_2Cl)_2$ was done entirely in a nitrogen glove bag in order to prevent exposure to either oxygen or water vapour. A preweighed portion was dissolved in toluene and impregnated onto an activated carbon support to incipient wetness. This sample was dried in the glove bag prior to being loaded into a sealed sample cell to allow easy transport and manipulation without fear of exposure to ambient conditions.

References

[1] Nefedov V I 1970 *J. Struct. Chem.* **4** 277
 Dehmer J L 1972 *J. Chem. Phys.* **56** 4496
 Agarwal B K, Bhargava C B, Vishnoi A N and Seth V P 1976 *J. Phys. Chem. Solids* **37** 725
[2] Chou S-H, Guo J and Ellis D E 1986 *Phys. Rev.* **34** 12; 1986 *J. Physique Coll. Suppl.* **47** C8
[3] Heitler W 1954 *The Quantum Theory of Radiation* 3rd edn (Oxford: Oxford University Press) p 179
 Agarwal B K 1983 *Quantum Mechanics and Field Theory* 2nd edn (Allahabad: Lokbhart) p 127
 Ogurtsov G N 1972 *Rev. Mod. Phys.* **44** 1
[4] Müller J E and Wilkins J W 1986 *Phys. Rev.* B **29** 4331
[5] Kutzler F W, Ellis D E, Morrison T I, Shenoy G K, Viccaro P J Montano P A, Appelmen E H, Stein L, Pellin M J and Gruen D M 1983 *Solid State Commun.* **46** 803
[6] Sayers D E, Stern E A and Lytle F W 1971 *Phys. Rev. Lett.* **27** 1204
 Stern E A and Sayers D E 1974 *Phys. Rev.* B **10** 3027
[7] Müller J E 1984 *EXAFS and Near Edge Structure III (Springer Proceedings in Physics 2)* ed K O Hodgson, B Hedm and J E Penner-Hahn (Berlin: Springer)
[8] Robota H J 1993 private communication
[9] Dill D and Dehmer J L 1974 *J. Chem. Phys.* **61** 692
 Dehmer J L and Dill D 1975 *Phys. Rev. Lett.* **35** 213
[10] Johnson K H and Smith F C Jr 1972 *Phys. Rev.* **831**
[11] Coey J M 1970 *Acta Crystallogr.* B **26** 1876
[12] Bärnighausen H and Handa B K 1964 *J. Less-Common Met.* **6** 226
[13] Dahl L F, Martell C and Wampler D L 1961 *J. Am. Chem. Soc.* **83** 1761
 Sakakibara T and Alper H 1979 *J. Chem. Soc. Commun.* 458
[14] 1992 *CRC Handbook of Chemistry and Physics* (Boca Raton, FL: Chemical Rubber Company) p E-191
[15] Sham T K 1983 *EXAFS and Near Edge Structure (Springer Series in Chemical Physics 27)* ed L Bianconi, S Incoccia and S Stipcich (Berlin: Springer) p 165
[16] Kawata S and Maeda K 1972 *J. Phys. Soc. Japan* **32** 778
[17] Nakamatsu H 1995 to be published
[18] Sham T K 1985 *Phys. Rev.* B **31** 1888, 1903
[19] Dahl J P and Avery J (ed) 1982 *Local Density Approximations in Quantum Chemistry and Solid State Physics* (New York: Plenum)
[20] Ellis D E and Painter G S 1970 *Phys. Rev.* B **2** 2887
 Delley B, Ellis D E, Freeman A J, Baerends E J and Post D 1983 *Phys. Rev.* B **27** 2132
[21] Goodman G L, Ellis D E, Alp E E and Soderholm L 1989 *J. Chem. Phys.* **91** 2983
[22] Guo J, Ellis D E, Alp E, Soderholm L and Shenoy G K 1989 *Phys. Rev.* B **39** 6125